

# A Numerical Study of Early Summer Regional Climate and Weather over LSA-East. Part I: Model Implementation and Verification

DA-LIN ZHANG AND WEI-ZHONG ZHENG

*Department of Meteorology, University of Maryland, College Park, College Park, Maryland*

YONG-KANG XUE

*Department of Geography, University of California, Los Angeles, Los Angeles, California*

(Manuscript received 15 May 2002, in final form 20 December 2002)

## ABSTRACT

The Pennsylvania State University–NCAR Mesoscale Model (MM5) and a simplified simple biosphere (SSiB) scheme are modified and then coupled to study various regional climate and weather problems. These modifications include correcting the moisture and cloud hydrometeor fields to ensure the mass conservation; incorporating the effects of dissipative heating to ensure total energy conservation; decoupling soil and vegetation types in specifying various surface parameters; and eliminating the shortwave radiation reaching the surface at points where deep convection occurs.

A 30-day integration of June 1998 over the Midwest states was used to examine the model's capability in capturing the observed wet regional climate and the passage of several mesoscale weather events. It is found that the coupled model reproduces the distribution and magnitude of monthly accumulated precipitation, the time series of area-integrated precipitation, surface pressures, and diurnal changes in surface temperatures, low-level winds and precipitation, as well as the evolution of precipitation systems across the central United States. In particular, the model reproduces well many daily weather events, including the distribution and intensity of low-level temperature and pressure perturbations and precipitation, even up to a month. The results suggest that the daily temperature, clouds, and precipitation events from the weekly to monthly scales, as well as their associated regional climate phenomena, could be reasonably simulated if the surface, boundary layer, radiation, and convective processes are realistically parameterized, and the large-scale forcing could be reasonably provided by general circulation models.

## 1. Introduction

Clouds and precipitation play an important role in determining the global and regional water and energy cycle. In addition, water vapor can be transported from one region to another through propagating cloud systems, and the associated precipitation can affect vegetation growth and the subsequent surface evaporation and even new cloud development. Precipitation can also modify the surface energy budget through changes in soil moisture and albedo.

Many of the previous modeling studies revealed that the hydrometeorological cycle would be enhanced in a warm climate setting with large variability in weather conditions (Houghton et al. 1996; Wetzel et al. 1996; Paegle et al. 1996). Despite the importance of cloud and precipitation in the regional water cycle, the progress in warm-season quantitative precipitation forecasts

(QPFs) has been slow due to the dominant weak dynamical forcing in the synoptic-scale environments and subgrid-scale meteorological forcing and surface conditions. Nevertheless, it is encouraging from recent real-data mesoscale modeling studies that the warm-season QPFs could be significantly improved in certain cases by simply incorporating high-grid resolution and realistic model (cloud and boundary layer) physics (Zhang and Fritsch 1988; Zhang et al. 1988; Stensrud and Fritsch 1994; Alexander and Cotton 1998). Similarly, recent regional climate modeling studies showed that the warm-season QPFs at the monthly to seasonal scales could be improved by using reasonable diabatic physics and land-surface parameterizations (Giorgi 1991; Xue et al. 1996b; Paegle et al. 1996). In particular, these studies showed that the warm-season precipitation at a timescale of a few days to weeks and beyond is extremely sensitive to the land-surface conditions. Even for a short-range QPF (e.g., 48 h), the impact of vegetation characteristics and land-surface processes could be pronounced (Xue et al. 2001), especially in regions with significant vegetation variations (Wen et al. 2000).

---

*Corresponding author address:* Dr. Da-Lin Zhang, Dept. of Meteorology, University of Maryland, College Park, College Park, MD 20742-2425.  
E-mail: dalin@atmos.umd.edu

Moreover, our ability of remotely sensing the characteristics of the land surface has been advanced dramatically in the past decade, allowing much better data to be input into the more sophisticated parameterizations (Loveland et al. 1991; Lee et al. 1995; Walko et al. 2000).

However, current general circulation models (GCMs) and most regional climate models use a grid resolution of over 50 km (e.g., Giorgi 1990, 1991; Browning 1994; Kiehl et al. 1996; Gong et al. 2000; Pan et al. 1999; Tsvetsinskaya et al. 2001; Small et al. 2001). Clearly, such numerical models could only treat clouds and precipitation in terms of relative humidity and some convective systems at the subgrid scale, and they will likely fail to predict rainbands, line convection, orographically driven precipitation, as well as their related meso- $\beta$ -scale circulations. Furthermore, some recent studies indicate that the spatial variability in precipitation and land-surface properties can significantly affect the simulated surface hydrological processes and that neglecting the spatial variability of rainfall may result in the misrepresentation of surface hydrological processes and surface energy balance (Ghan et al. 1997; Giorgi and Avissar 1997). Thus, it is highly desirable to examine the predictability of finescale precipitation events at the timescales of days up to a month and study the relative importance of key parameters involved in the rainfall production.

The issue of regional climate predictability is complicated due to the specification of lateral boundary conditions unless they are updated by GCM forecasts. However, even if the synoptic-scale atmospheric fields can be accurately specified along the lateral boundaries, we are still uncertain to what extent individual storm events and their pertinent precipitation (amount and distribution) could be reasonably predicted beyond a couple of days, and which is more important, precipitation or land-surface physics, in determining the individual storm predictability and regional climate conditions.

The objective of the present study is to address the above issues using a 30-day (i.e., 1–30 June 1998) continuous model simulation of regional climate over the large-scale area-east (LSA-E) that is defined as an area coverage from 89° to 78°W and from 33° to 43°N (see Fig. 1b). We are interested in this area because LSA-E is climatologically characterized by heavy precipitation that provides the dominant contribution to Mississippi River runoff, and by the pronounced influence of complex terrain on regional hydrometeorology and climate (GCIP 1996). To achieve the above objective, we incorporated the simplified simple biosphere (SSiB) scheme (Sellers et al. 1986; Xue et al. 1991) into the Pennsylvania State University–National Center for Atmospheric Research (PSU–NCAR) Mesoscale Model (i.e., MM5). An offline SSiB has been validated and calibrated using the data measured from various vegetation types and regions in the world (e.g., Xue et al. 1996a; Chen et al. 1996). Furthermore, the performance

of SSiB has been evaluated and compared to other land-surface schemes in the Project for Intercomparison of Land-Surface Parameterization Schemes (Henderson-Sellers et al. 1993; Yang et al. 1995; Shao and Henderson-Sellers 1996; Chen et al. 1997). Over the past decade, SSiB has also been extensively tested by the Center for Ocean–Land–Atmosphere Studies' (COLA) GCM, the National Oceanic and Atmospheric Administration–National Center for Environment Prediction's (NOAA–NCEP) GCM and Eta model, and the National Aeronautics and Space Administration Goddard Laboratory for Atmospheres' (NASA GLA) GCM for the coupled GCM and regional climate studies (e.g., Xue et al. 1991; 2001).

The next section describes the basic features of MM5 and SSiB, and their associated modifications, as well as their coupling. Section 3 compares the simulated area-averaged results to the observed at the daily to monthly timescales. Section 4 shows how well the model could reproduce some individual storm cases, as verified against observations. A summary and concluding remarks are given in the final section.

## 2. Model description

In this study, a modified version of the SSiB scheme is coupled with the PSU–NCAR MM5 model. The fundamental features of MM5 used for this study include (i) a two-way interactive, triply nested-grid technique with the finest 5-km resolution domain to cover the most part of the LSA-E (see Fig. 1b); (ii) the simultaneous use of the newest version of the Kain–Fritsch (1993) convective parameterization including the parameterized shallow convective effects (Deng et al. 2003) and an explicit moisture scheme (without the mixed phase) containing prognostic equations for cloud water (ice) and rainwater (snow) (Hsie et al. 1984; Zhang 1989; Dudhia 1989); (iii) the Blackadar planetary boundary layer (PBL) scheme (Zhang and Anthes 1982); (iv) a long- and shortwave radiation scheme that interacts with the atmosphere, clouds, and the surface (Dudhia 1989); and (v) the specification of the outermost coarse-mesh lateral boundary conditions by linearly interpolating NCEP's 6-hourly Eta-model analyses at the resolution of 40 km on the Advanced Weather Interactive Processing System (AWIPS) 212 grid according to Perkey and Kreitzberg (1976). Note that a convective parameterization is still used with a grid size of 5 km in the present case (see Table 1), because even the largest supercell storms (about 10 km  $\times$  10 km) would require a marginal grid size of 2.5 km to resolve with at least 4 grid points. In addition, our initial experimentations show the development of numerous mesocyclones with excessive precipitation even with the finest grid size of 3 km; this is very similar to that discussed in Zhang et al. (1988), Molinari and Dudek (1992), and Zhang et al. (1994). This implies that upward motion developed on this grid box still could not remove conditional in-

TABLE 1. The model grid design.

Domain	A (D1)	B (D2)	C (D3)
Dimensions (x, y)	95 × 72	109 × 94	181 × 157
Area coverage	4230 km × 3195 km	1620 km × 1395 km	900 km × 780 km
Grid size (km)	45	15	5

stability fast enough to prevent the development of conditional instability of the second kind (CISK)-like instability.

Table 1 describes the model grid design. A total of 31  $\sigma$  levels in the vertical are used with the model top at 50 hPa. These full  $\sigma$  levels are 0, 0.04, 0.08, 0.12, 0.16, 0.2, 0.24, 0.28, 0.32, 0.36, 0.4, 0.44, 0.48, 0.52, 0.56, 0.6, 0.64, 0.68, 0.72, 0.76, 0.8, 0.84, 0.87, 0.9, 0.92, 0.94, 0.958, 0.973, 0.985, 0.994, and 1, which give 30 half- $\sigma$  layers. The height of the lowest model layer, at which all the atmospheric variables except for vertical velocity are defined, is about 30 m. The outermost coarse-mesh domain, centered at 40.5°N, 95.0°W, is designed to be large enough such that the continental-scale dynamical forcing could be realistically propagated into the area of interest through the lateral boundaries.

#### a. Model improvements

While MM5 has demonstrated capability to simulate a wide range of weather phenomena [see the review by Anthes (1990)], there are two important additions and improvements that have been incorporated in order to obtain more realistic simulations of regional climate.

First, the moisture and cloud fields in MM5 tend to become negative, especially around the cloud boundaries, due to the use of the centered finite differencing. To avoid this problem, occurring mostly in the upper levels, these fields used to be set to a small positive value once they become negative. Obviously, this procedure does not conserve the domain-integrated precipitable water and could become a serious problem for climate simulations. In this study, we eliminate the negative values first by “transporting” moisture horizontally and vertically from the neighboring points. If sufficient moisture is available from these points, a local correction is made so that the other points are not affected. Since this procedure does not always eliminate negative moisture, any remaining negative values will then be eliminated by a “domain-borrowing” scheme similar to that used by Braun and Tao (2000). That is, the domain-integrated masses of negative and positive moisture are calculated, separately, and the positive moisture at all the other points will be decreased proportionally to offset the required increase of moisture. The same procedure is also applied to cloud hydro-meteors to ensure their conservation.

Second, the effects of dissipative heating, representing the sink of kinetic energy at the bottom boundary due to frictional dissipation, were neglected in MM5 as

in many of the other numerical models (Bister and Emanuel 1998; Zhang and Altshuler 1999). In order for total energy to be conserved, this kinetic energy loss due to frictional dissipation must be returned to the system as thermal energy. Zhang and Altshuler (1999) found the significant impacts of the dissipative heating on the surface sensible heat flux and cyclone intensity in a 72-h explicit simulation of Hurricane Andrew (1992). In the present study, the dissipative heating is incorporated, following Zhang and Altshuler (1999), and produces a warming of 0.2–0.3 K on a diurnal cycle (not shown). This warming gives rise of some notable differences in the one-month-accumulated precipitation.

#### b. The SSiB scheme and its improvements

The SSiB scheme is used to represent the land-surface processes in MM5. It has three soil layers and one canopy layer with eight prognostic equations: volumetric soil moisture content in the three soil layers; temperature in the canopy, ground surface, and deep soil layers; water stored in the canopy; and snow stored on the ground. Deardorff’s (1978) force–restore method is used to predict the fast response surface and the slow response deeper soil temperatures. In the three-layer soil model, water movement is described by a finite-difference approximation to the diffusion equations. The scheme describes 12 vegetation types, including tall and short vegetation, arable crops, and desert (Xue et al. 2001), each of which represents some average set of soil and vegetation characteristics.

There are three major components in the SSiB scheme: the calculations of albedo, aerodynamic resistances and surface resistances. These, along with the atmospheric and land-surface state variables, determine the radiative transfer and the momentum fluxes at the surface, and the partitioning of surface energy into sensible heat and latent heat fluxes. Three aerodynamic resistances in SSiB are used to compute the vertical eddy flux transfer between the vegetated surface and the reference height: the resistance between the soil surface and the canopy air space ( $r_a$ ); the resistance between all of the canopy leaves and the canopy air space ( $r_b$ ); and the resistance between the canopy air and the reference height ( $r_c$ ) (see Xue et al. 1991).

However, the iterative calculation of  $r_a$ , based on Monin–Obukhov similarity theory, does not always converge between the Richardson number, the canopy temperature, and  $r_a$ . In this study,  $r_a$  is calculated, following Zhang and Anthes (1982), based on the surface-layer stability and the PBL turbulence characteristics. This is

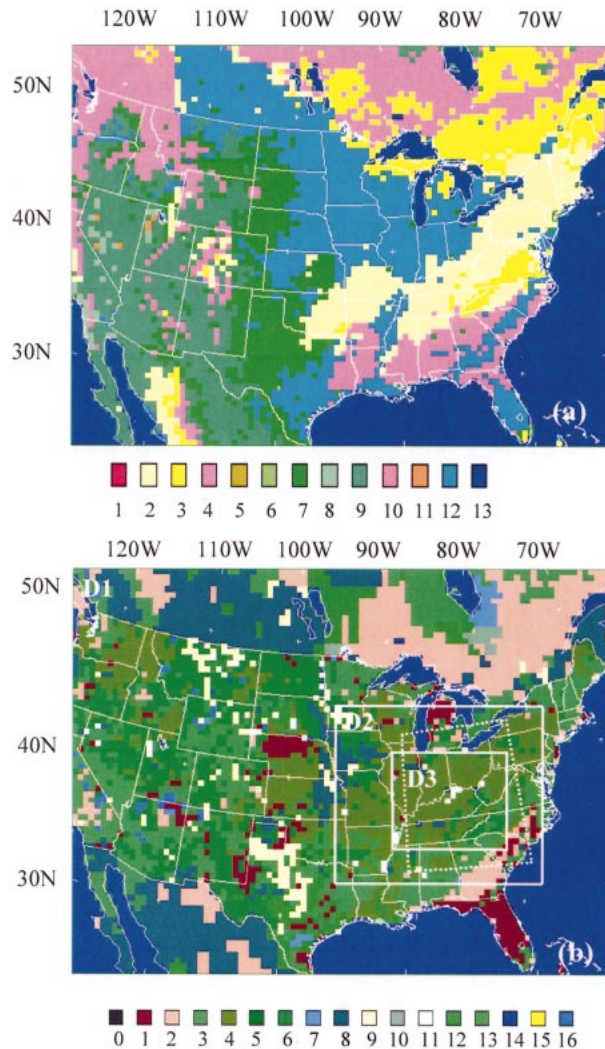


FIG. 1. Distribution of (a) the dominant vegetation types used with the lookup Table 2, and (b) the dominant soil types used with the lookup Table 3. The triply nested-grid domains (D1–D3), with the finer meshes denoted by the internal frames (solid lines), are also given. The dotted internal frame denotes the LSA-E area used for the area-averaged calculations in this study. Latitudes and longitudes are given every  $10^\circ$ .

done after the surface scaling parameters and the flux transfer coefficients are obtained. Our initial experimentations indicate that this modification not only eliminates oscillating and often divergent iterations, but also provides a more accurate description of the PBL.

In the original SSiB scheme, land-surface properties are specified according to the paired vegetation and soil types. In this study, we convert the 24 vegetation types from the U.S. Geological Survey (USGS) Earth Resources Observation Systems (EROS) 1-km resolution vegetation dataset to 13 types based on the description of SSiB; see Fig. 1a and a lookup Table 2. For each vegetation type in USGS its coverage fraction is not a constant but varies in accordance with the 5-yr monthly

climatology of green vegetation cover dataset derived from the advanced very high-resolution radiometer (AVHRR; Gutman and Ignatov 1998; Chen and Dudhia 2001). The coverage fraction of needle-leaf evergreen trees in June, for example, could range from 0.90 to 0.50 between the southern and northern parts of the North America, while in the original SSiB it is set to 0.75 everywhere. The soil types are determined independently from the 1-km resolution multiyear 16-category soil characteristics dataset developed by Miller and White (1998); see Fig. 1b and a lookup Table 3. Thus, the soil types, used to specify soil porosity, soil moisture potential,  $B$  parameter, and hydraulic conductivity at saturation in SSiB, are unpaired with the vegetation types. It is evident from Fig. 1b that in most areas one vegetation cover has different soil types, and vice versa.

The SSiB scheme is coupled with the Blackadar PBL scheme through the flux exchange between the ground and the surface air layer, as suggested by Xue et al. (2001), to ensure energy and momentum conservation across the land–air interface. In the coupled model, the diurnally varying surface albedo is calculated according to vegetation and soil properties, solar zenith angle, and snow. The surface albedo in turn influences the surface energy budget and skin temperature, which is closely related to canopy temperature and soil surface temperature. Wherever deep convection occurs, the shortwave radiation reaching the surface is set to zero to simulate the blocking effect of deep convective cloud on the high-resolution grid box.

### c. Model initialization and verification data

The model is initiated at 0000 UTC 1 June 1998 using the NCEP Eta model analyses and then integrated continuously for 30 days. The initial surface and canopy temperatures are also specified from NCEP's Eta analyses, that is, its 2-m altitude temperatures. The initial deep soil temperatures and moistures are interpolated to the SSiB soil layers both from NCEP's Eta analyses.

Two sets of precipitation measurements will be used to verify the model simulation: one is from the NCEP analysis, based on over 5000 rain gauge stations in the United States, at about  $0.25^\circ$  resolution; and the other is the hourly National Precipitation Analysis (NPA), based on multisensor (rain gauge and radar) measurements, at a 4-km resolution. The hourly digital precipitation (HDP) radar estimates are obtained from the Weather Surveillance Radar (WSR-88D) radar product generator on an array of  $131 \times 131$  with a 4-km resolution centered over each radar site. However, radar coverage and rain gauge observations are absent outside the United States and over oceans. It should be kept in mind that the retrieved radar rainfall rates tend to underestimate those observed by rain gauges.

With the above-mentioned state-of-the-art model physics and high grid resolution, we could anticipate

TABLE 2. Land-cover index and the SSiB vegetation types that correspond to the USGS vegetation types (and land-cover index).

Index	SSiB vegetation types	USGS vegetation types
1	Broad-leaf evergreen trees	Evergreen broad-leaf forest (13)
2	Broad-leaf deciduous trees	Savanna (10); deciduous broad-leaf forest (11)
3	Broad-leaf and needle-leaf trees	Mixed forest (15); wooded wetland (18)
4	Needle-leaf evergreen trees	Evergreen needle-leaf forest (14)
5	Needle-leaf deciduous trees	Deciduous broad-leaf forest (12)
6	Broad-leaf trees with ground cover	
7	Ground cover only	Urban and built-up land (1); grassland (7)
8	Broad-leaf shrubs with perennial ground cover	Mixed shrubland–grassland (9)
9	Broad-leaf shrubs with bare soil	Shrubland (8)
10	Dwarf trees and shrubs with ground cover	17; 20; 21; 22; 23*
11	Bare soil	Barren or sparsely vegetated (19)
12	Cultivations	2; 3; 4; 5; 6**
13	Water	Water (16)

\* This group includes herbaceous wetland (17), herbaceous tundra (21), wooded tundra (21), mixed tundra (22), bare ground tundra (23).  
 \*\* This group includes dryland cropland and pasture (2), irrigated cropland and pasture (3), mixed dryland–irrigated cropland and pasture (4), cropland–grassland mosaic (5), cropland–woodland mosaic (6).

the coupled MM5–SSiB model to be capable of capturing major rainfall events, because the large-scale circulation driven by the outermost coarse-mesh solution determines the paths, frequency, and intensity of the cyclones/fronts crossing the region, while important local surface climatic forcings, for example, the heterogeneous surface fluxes and finescale orographically generated circulations, provide the important mechanisms for triggering deep convection and for supplying the energy needed in the storm development.

### 3. Regional climate simulations

In this section, we focus mainly on the daily to monthly simulatability of area-averaged meteorological properties over the LSA-E in the month of June 1998. This region experienced the passage of seven cyclones and a few mesoscale convective systems (MCSs) during June 1998, causing the regional widespread anomalous precipitation with local flooding conditions. In fact, an examination of “*Weekly Weather and Crop Bulletin*” reveals that June 1998 was the wettest month for the

region since the great flood of June–August 1993. Most of the precipitation seemed to be convective in nature and generated by the frontal lifting and local surface conditions. The associated low-level climate setting is given in Fig. 2, which shows typically two major air-streams meeting over the northern Great Plains on the east side of the Rocky Mountains: one strong south-to-southwesterly flow carrying the warm (moist) air from the Gulf of Mexico and the other weak west-to-northwesterly flow advecting the cold (dry) air of the Arctic origin along the eastern edge of the Rocky Mountains. [The southwestern portion of the warm air is associated with the elevated heat source over the high plateau of Mexico, as discussed by Carlson et al. (1983)]. As a result, a moderate temperature gradient appeared in the southwesterly warm (and moist) flow that extends from Oklahoma to the LSA-E. Most of the clouds and precipitation events were observed to develop near the interface between the two different airflows, which was, on average, displaced gradually northward during the month. While the Gulf of Mexico was the moisture source for the major precipitation events, relative humidity increased toward the colder air (Fig. 2), partly as a result of extensive precipitation.

To examine the simulatability of regional climate we compare first the simulated daily averaged precipitation to the observed with the two different types of measurements (see Fig. 3). Apparently, both the simulation and observations exhibit pronounced spatial variability in the rainfall distribution with the daily averaged rainfall ranging from 2 to 7 mm day<sup>-1</sup> or 60–210 mm month<sup>-1</sup>. To facilitate our examination of the model simulatability, major rainfall regions are labeled with various letters in Figs. 3a–c. Heavier rainfall (i.e., >7 mm day<sup>-1</sup>) was observed from western Missouri (MO) to the eastern West Virginia (WV), and from northern Iowa (IA) down to Tennessee (TN). Although Figs. 3a and 3b were obtained from different measurements, the general rainfall patterns and magnitudes are consistent

TABLE 3. Description of soil index and soil types.

Index	Soil types
1	Sand
2	Loamy sand
3	Sandy loam
4	Silt loam
5	Silt
6	Loam
7	Sandy clay loam
8	Silty clay loam
9	Clay loam
10	Sandy clay
11	Silty clay
12	Clay
13	Organic materials
14	Water
15	Bedrock
16	Other (land ice)

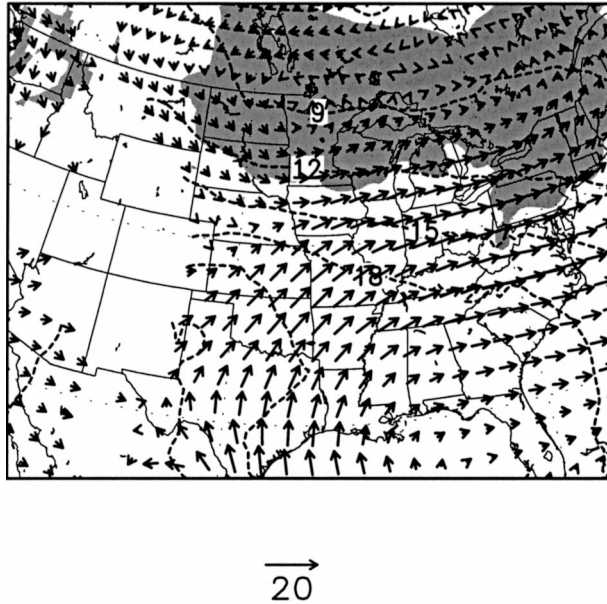


FIG. 2. Distribution of the monthly averaged horizontal flow vectors, temperatures (dashed lines), and relative humidity ( $>70\%$  shaded) at 850 hPa from the 30-day simulation. Areas underneath the mountains have been masked.

with each other, and they only differ slightly over some regions due likely to their different data resolutions or lack of observations. Nevertheless, the radar–gauge composite has significantly more finer-scale structures (Fig. 3b).

In general, the coupled MM5–SSiB model captures very well the distribution and magnitude of precipitation (cf. Figs. 3a–c). For example, the model reproduces heavy rainfall over areas IA, MO, IN, and WV. However, the model appears to underestimate rainfall somewhat over TN, and may overestimate it over the Appalachians (area AM). The latter discrepancy is likely caused by the lack of measurements over this mountainous region (i.e., area AM). The heavy rainfall over areas WV and AM is clearly topographically forced on the upwind side of the Appalachians Mountains. Of particular interest is that most of the weather systems tend to reduce rainfall amount and likely diminish after passing the mountainous regions, as suggested by both the observations and simulation (cf. Figs. 3a–c). This appears to suggest the effect of the Appalachians on the enhanced (decreased) precipitation on the upwind (downwind) side of the mountains.

Figure 4 compares the daily precipitation averaged over the LSA-E in a time series. The seven major weather systems (i.e., A–G) across the LSA-E produced a significant amount of precipitation during the month, with the heaviest rainfall events occurring on 5 June. The model reproduces the four continuous rainfall periods, for example, from days 1 to 8, days 8 to 18, days 18 to 25, and the final five days. Individual rainfall events are also reasonably captured, except for events

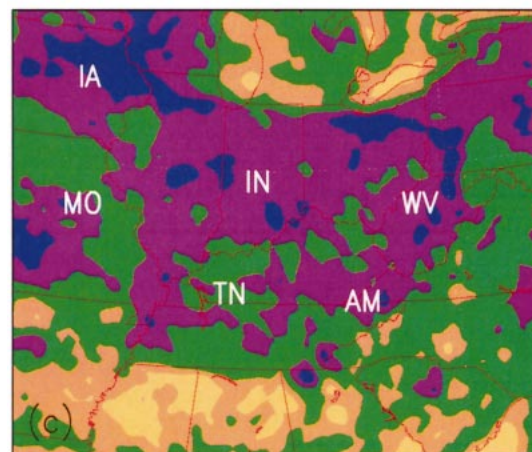
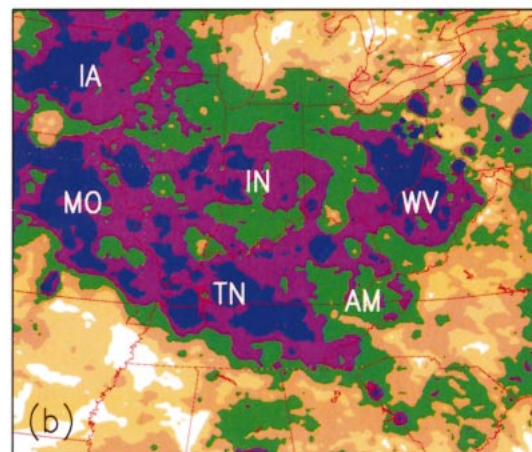
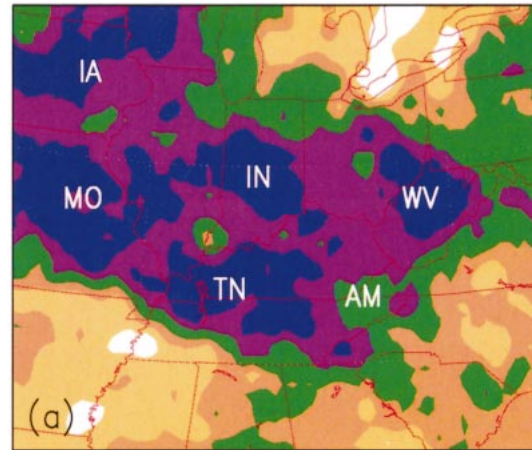


FIG. 3. Comparison of the daily averaged rainfall amount ( $\text{mm day}^{-1}$ ) over the 1–30 Jun 1998 period between (a) the daily rain gauge measurements at  $0.25^\circ$  resolution; (b) the NCEP hourly multisen- soring measurements at 4-km resolution; and (c) the simulated. The letters “IA,” “MO,” “IN,” “WV,” “TN,” and “AM” are used to represent various heavy rainfall areas over Iowa, Missouri, Illinois, West Virginia, Tennessee, and the Appalachians, respectively, for the sake of the model verification.

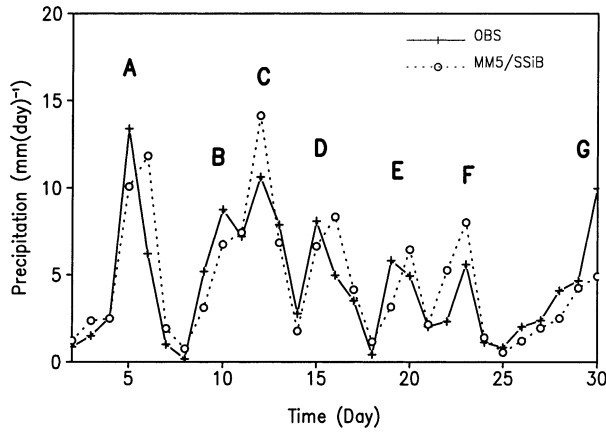


FIG. 4. Time series of the LSA-E area-averaged daily accumulated precipitation (mm) for the observed (solid) and the simulated (dotted) from 1200 UTC 1 Jun to 1200 UTC 30 Jun 1998. The LSA-E area is enclosed from 89° to 78°W and 33° to 43°N. The letters “A”–“G” denote the passage of major weather systems or events over the region for the convenience of discussions in the text.

D and E in which the simulated rainfall lags behind the observed by 1 day. The model reproduces the two heavier rainfall events A and B in the first 11 days in both magnitude and phase, which may be as expected. However, the model also simulates event G even at the end of 30-day integration, indicating the significant degree of regional climate simulatability. Some errors in the simulated rainfall amounts can be noted (e.g., in events C, F, and G).

A comparison of Figs. 4 and 5 reveals that these regional rainfall events were closely related to the passages of five major low pressure systems, except for event F, which was associated with several high-frequency disturbances superimposed on a high pressure system. For example, the largest 24-hPa regional pressure drop, occurring during 8–15 June, resulted from the propagation of one weak and one deep trough, followed by a closed low at 500 hPa (NCEP 1998); they were responsible for the continuous rainfall events B,

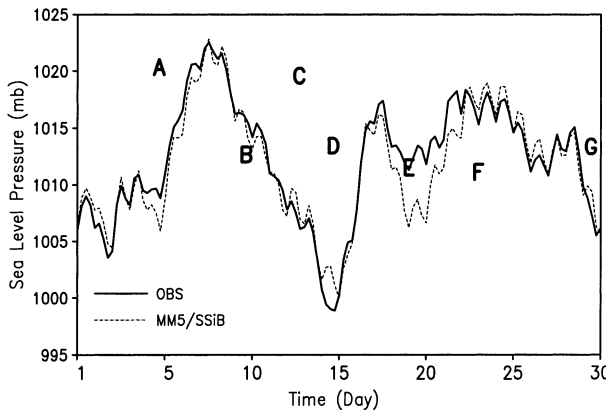


FIG. 5. As in Fig. 4, except for the 6-hourly sea level pressures from the observed (solid) and the simulated (dashed).

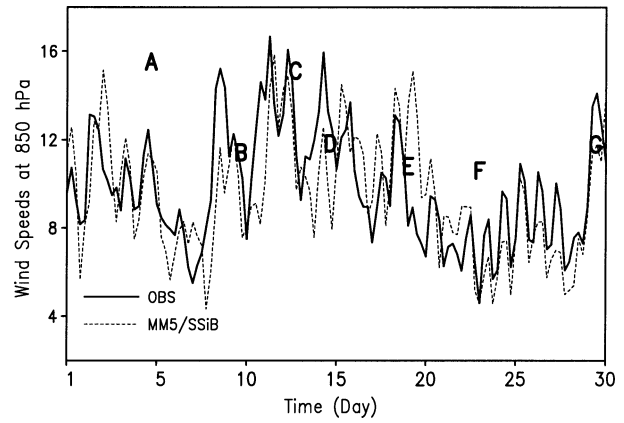


FIG. 6. As in Fig. 4, except for the 6-hourly horizontal wind speeds at 850 hPa (solid, observed; dashed, simulated).

C, and D, respectively. All precipitation events diminished rapidly as the regional pressure increased. The 3-hourly observations also show the passages of various high-frequency (roughly at the daily timescale) disturbances across the LSA-E, superposed on the propagating deepening pressure systems. Apparently, the model reproduces the time series of the area-averaged pressure, including the frequency and phase of the small-scale disturbances. The model-simulated large amplitudes of the high-frequency disturbances in some cases are considered realistic because of the higher grid resolution used than that in observations. However, there are notably larger pressure differences (~3 hPa) between the simulated and observed in events D and E due to misplaced cyclone centers; they appear to explain the relatively larger errors in magnitude and phase in the regional rainfall (cf. Figs. 3 and 4) as well as those in other meteorological fields (e.g., surface temperatures). Nevertheless, the reasonable agreement of the simulated regional pressure systems with the observed, which

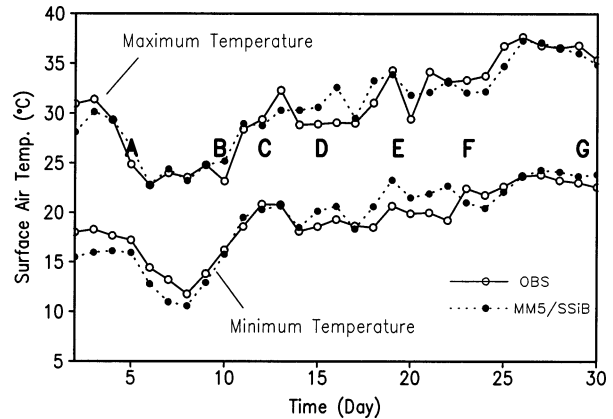
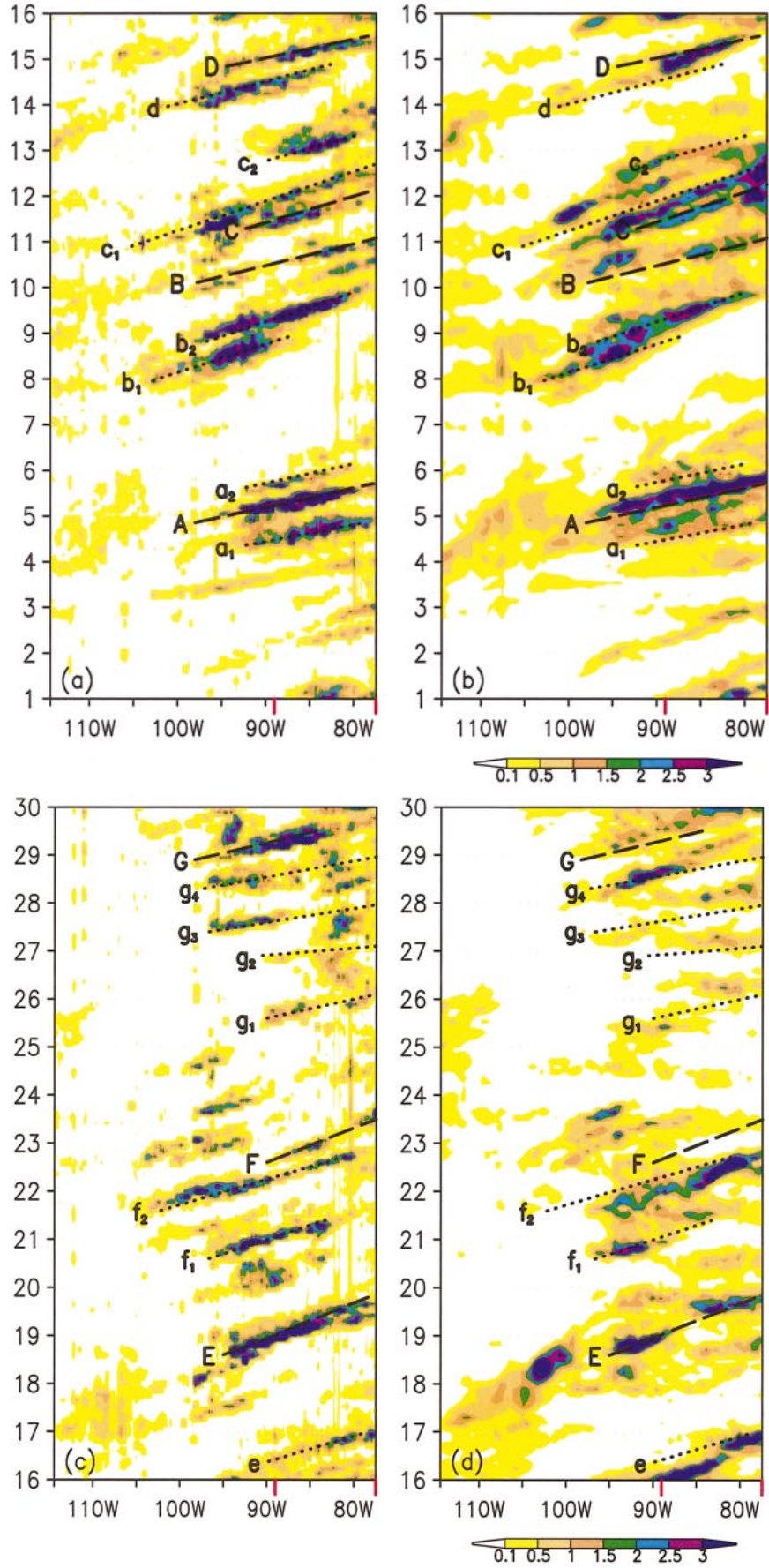


FIG. 7. As in Fig. 4, except for the daily maximum and minimum surface temperatures from the observed (solid) and the simulated (dotted). Note that the surface temperatures are defined herein as those underneath canopy from the SSiB scheme (see Xue et al. 1991, 2001).



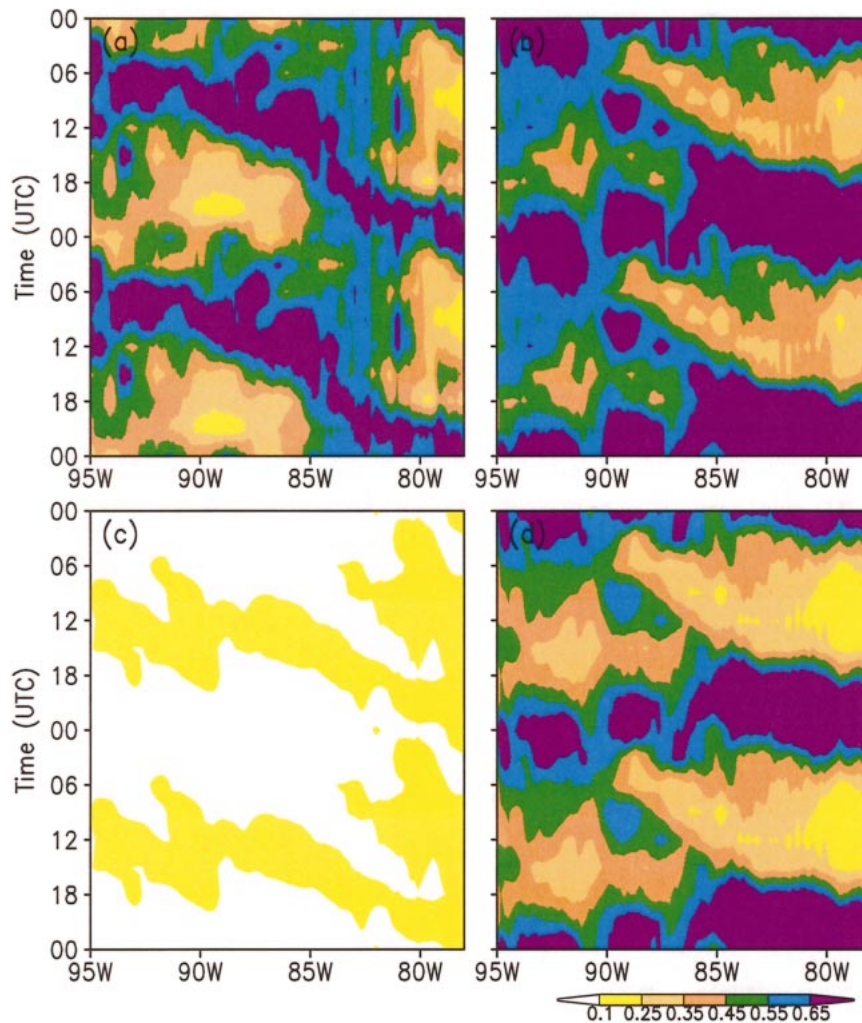


FIG. 9. Diurnal variation (in terms of UTC) of rainfall in  $\text{mm (3 h)}^{-1}$  along the longitude  $95^{\circ}$ – $78^{\circ}$ W averaged over the belt of  $33^{\circ}$ – $43^{\circ}$ N and over the period of 1–30 Jun 1998 from (a) the NCEP hourly multisensor analyses, (b) the simulated total rainfall, (c) the simulated grid-scale rainfall, and (d) the simulated convective rainfall.

could be attributed partly to the specified lateral boundary conditions, is a prerequisite for reproducing the observed rainfall events, since these large-scale pressure disturbances provide favorable environments for the development of clouds and precipitation.

Figure 6 compares the area-averaged horizontal winds at 850 hPa between the observed and simulated. In general, the strength of the regional low-level winds corresponded roughly to the regional rainfall events (cf. Figs. 6 and 4), but their oscillative frequencies appeared

to exhibit diurnal variations associated with the PBL and deep convection that were modulated by propagating pressure perturbations (cf. Figs. 6 and 5). It follows that both the local and large-scale forcings play important roles in determining the amplitude and phase of regional flows. Again, the model reproduces well the regional winds, except for portions of events D and E in which there are  $4$ – $6 \text{ m s}^{-1}$  errors in wind speed. However, the diurnal phase of the low-level winds is well reproduced, which coincides with the area-aver-

←

FIG. 8. Comparison of the time-zonal (from  $115^{\circ}$  to  $78^{\circ}$ W) cross section, or “Hovmöller diagram,” of 3-hourly rainfall rates [ $\text{mm (3 h)}^{-1}$ , shaded] averaged over the belt of  $33^{\circ}$ – $43^{\circ}$ N between (left) the observed and (right) the simulated: (a), (b) for the first half-month of Jun 1998; (c), (d) for the second half-month. Capital letters “A”–“G” used with dashed axes denote major weather systems over the region (see Fig. 4), whereas small letters “a”–“f” used with dotted axes represent their associated subsystems. The LSA region is indicated by a thick solid line along the abscissa. (b), (d) Dashed and dotted axes are duplicated from (a) and (c) for the convenience of model verification.

aged high-frequency pressure perturbations. As will be shown in a forthcoming journal article, this diurnal wind variation could be attributed to the use of the Blackadar PBL scheme. Four other PBL schemes, which are currently available in MM5, are unable to reproduce the diurnal cycle of the low-level winds.

Because of the reasonably simulated regional precipitation, the model reproduces the time series of the regional maximum and minimum surface air temperatures during the month (see Fig. 7). On average, the regional temperature difference between the observed and simulated is less than  $1.5^{\circ}\text{C}$ , except for days 16 and 22 on which the simulated maximum and minimum surface temperatures are about  $3^{\circ}\text{C}$  warmer than the observed, respectively. The simulated warmer temperature is likely due to the generation of less surface evaporation associated with the phase error in the cyclone center and its associated precipitation (cf. Figs. 4, 5, and 7). The model also simulates well the amplitude of diurnal changes (i.e., from  $7^{\circ}$  to  $13^{\circ}\text{C}$ ) with a warming trend toward the July month. The changes in the diurnal temperature amplitude are reasonably correlated with the precipitation events (cf. Figs. 4 and 7).

Let us next examine the ability of the model to simulate temporal evolution of individual rainfall systems within a latitudinally averaged belt across the  $33^{\circ}$ – $43^{\circ}\text{N}$ , given in Fig. 8, which is often referred to as the Hovmöller diagram. This  $33^{\circ}$ – $43^{\circ}\text{N}$  latitudinal average includes a sizeable amount of precipitation and its associated weather events (cf. Fig. 3), while the 3-hourly time series resolves the development of many semidiurnal and higher-frequency storms. A similar approach has been used by Carbone et al. (2002) to study a radar-based climatology of warm-season precipitation episodes. They found many coherent rainfall patterns with some zonally propagating characteristics. In general, Figs. 8a–c exhibit numerous rainfall streaks propagating in this zonal belt that are similar to those shown in Carbone et al. (2002). Of interest is that some rainfall streaks were initiated at the foothills of the Rocky Mountains during the first 18 days (Fig. 8a) whereas there was little convective activity subsequently over this semiarid region (Fig. 8c). These rainfall events to the west of  $105^{\circ}\text{W}$  were mostly quasistationary and diurnally forced, namely, occurring near late afternoons. Some rainfall systems, developed at the Rockies' foothills, appeared to propagate downstream (e.g.,  $b_1$ ,  $c_1$ , and d). But most rainfall streaks were either initiated or entered into the  $33^{\circ}$ – $43^{\circ}\text{N}$  latitudinal belt from outside near  $100^{\circ}\text{W}$ , and then they propagated eastward. Only a few systems survived more than one diurnal cycle (e.g., C, d, E) while the others either diminished within this belt or moved out. The rainfall streaks  $c_1$ , d, and E lasted the longest, from the Rockies to the Appalachians, with durations of 39–42 h. There also existed numerous short rainfall streaks to the west of the LSA-E. Nevertheless, most of the rainfall streaks diminished as they approached  $79^{\circ}\text{W}$ , which is consistent with the

early finding that precipitation decreased significantly after passing the Appalachians (cf. Figs. 3 and 8a,c). Over the LSA-E, numerous short-lived rainfall streaks were generated with a life cycle of less than 12 h (e.g., B,  $C_2$ , e,  $g_1$ , and several unlabeled streaks). As mentioned earlier, all the rainfall streaks coincided reasonably well with the passages of various high-frequency atmospheric disturbances in the region (cf. Figs. 5, 6, and 8). However, there is little indication of westward-propagating rainfall and weather systems as noted by Carbone et al. (2002).

To facilitate verification of the simulated rainfall streaks against the observed, the observed rainfall axes are superposed with the simulated rainfall (cf. Figs. 8a,c and 8b,d). It is apparent that the coupled model reproduces the generation and propagation of almost all the rainfall streaks except for the timing of a few rainfall events (e.g.,  $a_1$ , B,  $c_1$ , d, e,  $f_2$ , and F). The general locations in longitude, duration, and propagating speed are also well simulated. The model reproduces the initiation of light rainfall on the foothills of the Rockies during the first 18 days and little precipitation afterward. Of interest is that the model simulates the diurnally forced precipitation everyday during the period of 7–14 June; this appears to be closely related to the accumulated heavy rainfall in the second week (cf. Figs. 8a,b and 3). This can also be seen from the observed except for weaker continuity of radar-derived rainfall traces. Of further interest is that the model reproduces the frequency of rainfall events over the LSA-E, varying from twice a day (e.g.,  $b_1$  and  $b_2$ ) to little rainfall in 2–3 days (e.g., 6–8 June and 23–25 June). In addition, the model simulates relatively faster propagation of rainfall streaks over the LSA-E in the first 2–3 weeks and slower movements of storms in the final week. Both the observations and simulation even show quasistationary rainfall streaks (e.g.,  $g_2$ ,  $g_3$ , and  $g_4$ ) in the final week, as a result of diurnal forcing as approaching to the summer month of July (see Figs. 8c,d).

Figures 9a,b compare the diurnal variations of temporally and spatially averaged rainfall of the simulated to the observed, with the frequency Hovmöller diagrams similar to Fig. 12 given in Carbone et al. (2002). Significant diurnal variations of precipitation are evident across the longitudes of  $95^{\circ}$ – $78^{\circ}\text{W}$ . Of interest is that the maximum rainfall occurs at late night (i.e., 0400–1200 UTC) for regions to the west of  $87^{\circ}\text{W}$ , whereas to its east more rainfall tends to develop during the daytime (i.e., 1200–0000 UTC) and mostly the afternoon hours as moving toward the eastern boundary (Fig. 9a). Moreover, a secondary rainfall maximum, mostly nocturnal, appears from  $95^{\circ}$  to  $81^{\circ}\text{W}$ . These regions of heavy nocturnal rainfall are consistent with those found by Wallace (1975). It is encouraging that the model reproduces the nocturnal heavy rainfall to the west of  $87^{\circ}\text{W}$  and the afternoon peak precipitation to its east (cf. Figs. 9a,b). However, MM5 produces a 3–5-h shift toward the early evening in the nocturnal peak over the

95°–91°W region, and two rainfall peaks (i.e., during the 1800–0000 and 0800–1200 periods, respectively) over the 90°–87.5°W region. In addition, the model produces only a portion of the secondary rainfall maximum. A decomposition of the total rainfall indicates that over 95% of the precipitation is convective in nature (cf. Figs. 9b–d), and the model appears to produce too much afternoon rainfall to the west of 87°W (Fig. 9d). Based on the previous modeling studies of Zhang and Fritsch (1988) and Zhang and Gao (1989), it appears that convectively generated moist downdrafts play an important role in reproducing the sustained nocturnal convective precipitation. Our sensitivity simulations, to be shown in a future paper, also indicate the importance of the PBL and land-surface processes in generating the diurnal variations of the observed precipitation.

In summary, the coupled model is capable of simulating many regional climate features, such as the area-averaged precipitation, horizontal winds, surface temperatures (maximum and minimum), and pressures at the daily to monthly timescales, as well as the diurnal variations of precipitation. The latitudinally averaged cloud and precipitation fields in a time series could also be reasonably simulated.

#### 4. Climate case studies

While the results given in the preceding section show the model's excellent capability in capturing the spatially or temporally averaged rainfall events, it is unclear to what extent the coupled model can reproduce individual weather events on daily to monthly timescales. Of course, because of the long-period integrations, the simulated weather systems/conditions may not necessarily be verifiable at the right timings and locations. Here, four rainfall events (i.e., A, C, F, and G) with different characteristics are selected, based on Figs. 4 and 5, to demonstrate how well the observed low-level pressure systems and their associated daily rainfall are individually simulated (Figs. 10–13), given the reasonable larger-scale flows at the lateral boundaries. To help understand the evolution of these rainfall events, NCEP's daily maps (NCEP 1998), *Weekly Weather and Crop Bulletin*, and twice-daily satellite imagery archived at NOAA/National Climate Data Center are used to provide the necessary descriptions and verifications.

First, from 0000 UTC 2 June to 0000 UTC 6 June, a southwest–northeast-oriented cold front with two cyclone centers (initially, one at Lake Michigan, and the other in central South Dakota) moved southeastward through the LSA-E and gradually merged into a west–east-oriented quasistationary front, which appeared as a trough with significant meridional temperature gradients at 850 hPa (Fig. 10a) in the central LSA-E. This frontal system generated light precipitation ahead and to the north of the LSA-E (Fig. 10a). However, the merging process spawned an intense MCS (i.e., A in Fig. 8a) that propagated eastward on the southern side

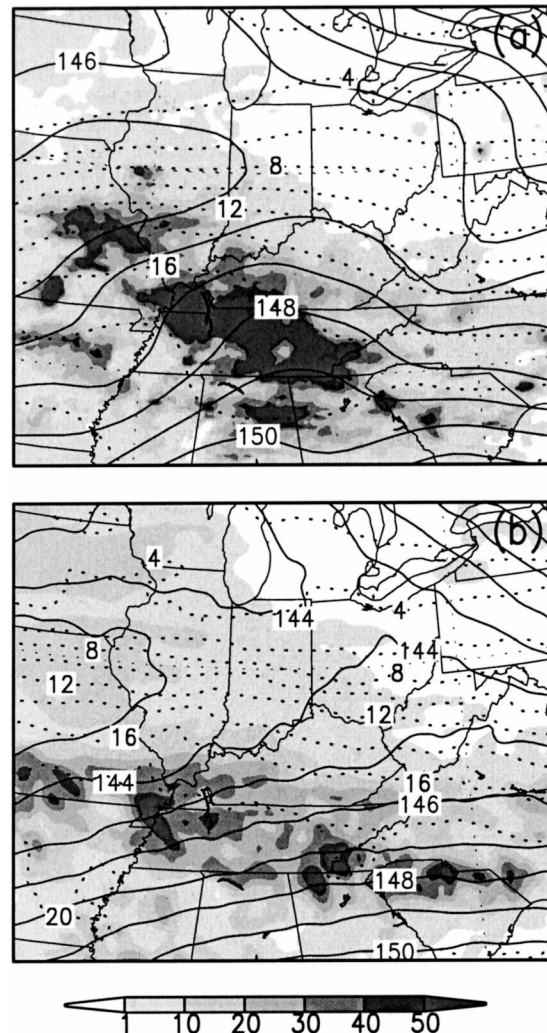


FIG. 10. Comparisons of the daily averaged (i.e., from 1200 to 1200 UTC) geopotential height (solid) at intervals of 10 m and temperature at intervals of 2°C at 850 hPa, and rainfall amount (shaded) between (a) the observed and (b) the simulated for event A on 5 Jun 1998.

of the front, leaving behind heavy rainfall mostly over Tennessee. Deep convection continued until the MCS moved into the Florida peninsula.

The model simulates well the overall pattern and most of the details in the precipitation, temperature, and height fields of event A (cf. Figs. 10a,b). As compared to the observation, however, the model produces a slightly deeper trough with a stronger meridional height gradient associated with the frontal system. On the other hand, the deeper trough may be attributed to the use of high grid resolution, causing more grid-scale precipitation and more rapid spinup of a cyclone. Despite the different amplitudes of the troughs, the model reproduces the magnitude and distribution of heavy precipitation over Tennessee with a slight different orientation. The 24-h accumulated rainfall is more than 50 mm over

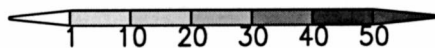
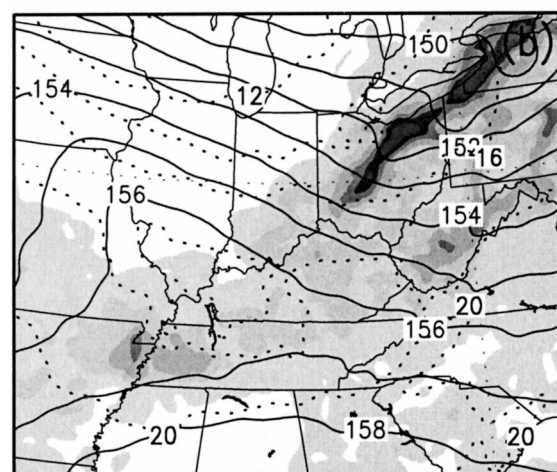
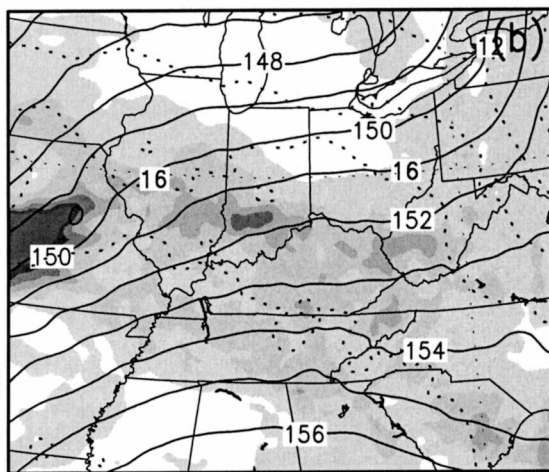
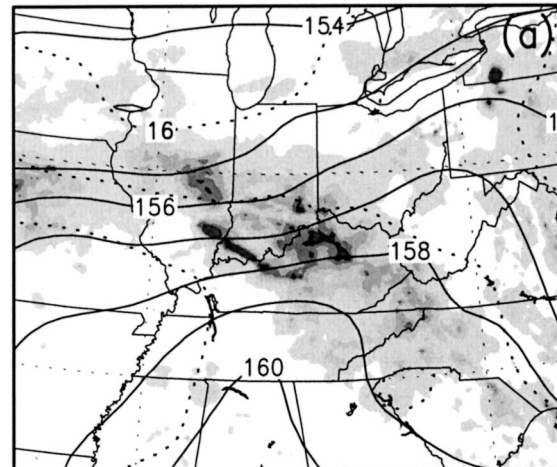
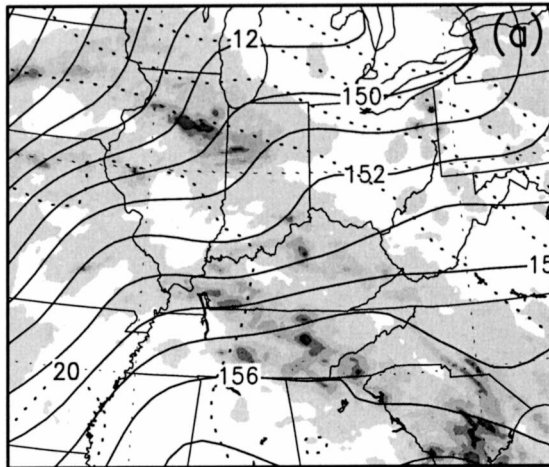


FIG. 11. As in Fig. 10, but for event C on 11 Jun 1998.



FIG. 12. As in Fig. 10, but for event F on 23 Jun 1998.

most of Tennessee from both the observations and simulation. An examination of 3-hourly maps (not shown) indicates that the model also reproduces fairly well the passage of several storms over the LSA-E, that is, A,  $a_1$ , and  $a_2$  as given in Fig. 8.

As mentioned earlier, three major midlevel cyclonic systems passed over the LSA-E during the 8–15 June period when the regional pressure kept falling (Fig. 5). The model-simulated rainfall and height fields associated with the third storm C, beginning on 11 June, are compared to the observed in Figs. 11a,b. This storm developed ahead of a midlevel deep trough with a cyclone located over the Great Lakes area. Widespread precipitation occurred along a northwest–southeast (NW–SE)-oriented warm front that swept northeastward through the LSA-E. This storm generated more than 40-mm daily precipitation over the region (Fig. 11a). In general, the model reproduces the basic structure and intensity of the low- to midlevel disturbances, including

the orientation of isobars, weak thermal gradients in the midwest states (cf. Figs. 11a,b). The simulated distribution and magnitude of precipitation also compare favorably to the observed. Clearly, the baroclinic forcing provided by the midlevel deep trough helps reproduce the regional flows and precipitation, although the model physics schemes appear to have also played important roles in determining the simulation quality.

Perhaps the least predictable storm is the sixth one (i.e., F) that developed in a dynamically weak environment on 23 June, as compared to the other storms (cf. Figs. 5 and 12a,b). This is a transition period to the summer month during which the subtropical high began to progress into the North American continent, and the low-level flow was characterized by a high pressure system over the southeastern states (Fig. 12a). An MCS developed on 22 June along a west–east-oriented quasi-stationary front that meandered in the northern LSA-E region until 0000 UTC 25 June and produced signif-

icant precipitation over the region (Fig. 4). Although the model reproduces the area-averaged rainfall in terms of magnitude and phase, its simulated rainfall pattern and isobar distribution differ from the observed (cf. Figs. 12a,b). A further verification against the 3-hourly analyses reveals that the simulated low-level system moves faster than the observed by 4–6 h due likely to the absence of the southeastern high (Fig. 12b) that tends to slow the movement of the mesolow. Nevertheless, the rainfall and height distributions compare favorably to the observed when the two are compared with the 6-h difference considered (not shown).

Near the end of June 1998, the subtropical anticyclonic flow with weak gradient dominated most of the United States in the low- to mid troposphere (NCEP 1998). An MCS developed over central Iowa ahead of a weak cold front. It brought widespread moderate to localized heavy rain into the LSA-E on 29–30 June (Fig. 13a), with pronounced surface pressure perturbations and outflow boundaries along its southeastward-oriented path. The model simulates very well the orientation and magnitude of isobars and isotherms at 850 hPa, and reasonably well the gross distribution and widespread light precipitation over the region (cf. Figs. 13a,b). Some errors in the location of the heavier NW–SE-oriented rainfall band can be noted.

The above results indicate that the coupled MM5 can simulate individual mesoscale weather events, particularly associated with extratropical cyclones/fronts, even at the monthly timescale. However, the model tends to have less predictability for convective developments under weak gradient environments. Although the specified lateral boundary conditions, which restrain error growth in the large-scale forcing (Anthes et al. 1985; Warner et al. 1997), help undoubtedly reproduce the observed mesoscale weather events, various parameterized physical processes (e.g., diabatic heating, PBL, land-surface fluxes, and topography, in that order) must play an important role in determining where and when they would occur and the distribution of their associated precipitation. This will be shown in a forthcoming journal article.

## 5. Summary and conclusions

In this paper, modifications of the PSU–NCAR mesoscale model and the SSiB land-surface scheme and their coupling, used to study the regional climate and weather on the daily to monthly timescales, are documented. These modifications include (i) correction of the moisture and cloud hydrometeors fields, when becoming negative, to ensure the mass conservation; (ii) the effects of dissipative heating to ensure total energy conservation; (iii) calculation of the resistance between the canopy air space and the reference height, following Zhang and Anthes (1982), based on the surface-layer stability and the PBL turbulence characteristics; (iv) the soil types that are unpaired with the vegetation types

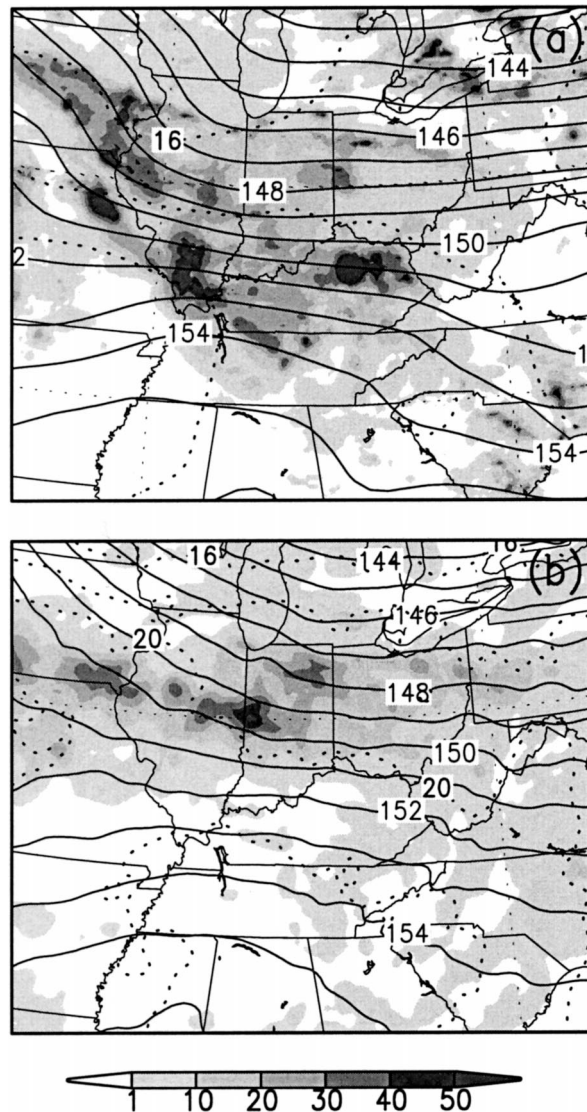


FIG. 13. As in Fig. 10, but for event G on 30 Jun 1998.

(both at 1-km resolution) in specifying various surface parameters to provide more realistic description of surface fluxes; and (v) the shortwave radiation reaching the surface is set to zero wherever deep convection occurs to simulate the blocking effect of deep convective cloud on the high-resolution grid box.

A 30-day integration of the wet month of June 1998 over LSA-E was selected to examine the model's capability in simulating various regional climate and weather phenomena. Compared to available observations, the coupled model reproduces many regional climate features, such as the distribution and magnitude of monthly accumulated precipitation, the time series and diurnal variation of area-integrated precipitation, surface pressures, and maximum and minimum surface temperatures, as well as the low-level winds. In particular, the model simulates fairly well the timing and pas-

sage, including frequency and intensity, of several convective storms over the region in terms of pressure perturbations and regional clouds and rainfall. The simulated propagation and generation of rainfall systems across the central United States (and LSA-E) during the month are very similar to the observed.

Of more significance of this study is that the model reproduces well not only the regional climate features at weekly to monthly scales, but also many daily weather events (e.g., the distribution and intensity of precipitation and low-level temperature and pressure perturbations), even up to a month. This is particularly true for those MCSs associated with extratropical cyclones/fronts. A series of sensitivity simulations, to be shown in a forthcoming journal article, indicates that the physics options chosen from MM5 and the improved physics processes play important roles in determining the ability to simulate these regional climate and weather features. Thus, we may conclude that the daily temperature, low-level winds, clouds, and precipitation events, as well as their associated regional climate (weekly to monthly) phenomena, can be reasonably predicted if the large-scale forcing could be reasonably provided by GCM models and if realistic parameterizations of the surface, PBL, convective processes, and longwave and shortwave radiation could be incorporated into regional numerical weather prediction models.

*Acknowledgments.* We thank Dr. Wei-Kuo Tao at NASA for his helpful discussions on the conservation of moisture, Dr. Ying Lin at NOAA/NCEP for providing the 4-km resolution precipitation data, and three anonymous reviewers for their helpful comments. This work was supported by NOAA Grants NA96GP0277 and NA16GP1581.

#### REFERENCES

- Alexander, G. D., and W. R. Cotton, 1998: The use of cloud-resolving simulations of mesoscale convective systems to build a mesoscale parameterization scheme. *J. Atmos. Sci.*, **55**, 2137–2161.
- Anthes, R. A., 1990: Recent applications of the Penn State/NCAR mesoscale model to synoptic, mesoscale, and climate studies. *Bull. Amer. Meteor. Soc.*, **71**, 1610–1629.
- , Y.-H. Kuo, D. P. Baumhefner, R. M. Erico, and T. W. Bettge, 1985: Predictability of mesoscale atmospheric motions. *Advances in Geophysics*, Vol. 28, Academic Press, 159–202.
- Bister, M., and K. A. Emanuel, 1998: Dissipative heating and hurricane intensity. *Meteor. Atmos. Phys.*, **55**, 233–240.
- Braun, S. A., and W.-K. Tao, 2000: Sensitivity of high-resolution simulations of Hurricane Bob (1991) to planetary boundary layer parameterizations. *Mon. Wea. Rev.*, **128**, 3941–3961.
- Browning, K. A., 1994: Survey of the perceived priority issues in the parameterization of cloud-related processes in GCMs. *Quart. J. Roy. Meteor. Soc.*, **120**, 483–487.
- Carbone, R. E., J. D. Tuttle, D. A. Ahijevych, and S. B. Trier, 2002: Inferences of predictability associated with warm season precipitation episodes. *J. Atmos. Sci.*, **59**, 2033–2056.
- Carlson, T. N., S. G. Benjamin, and G. S. Forbes, 1983: Elevated mixed layers in the regional severe storm environment: Conceptual model and case studies. *Mon. Wea. Rev.*, **111**, 1453–1473.
- Chen, F., and J. Dudhia, 2001: Coupling an advanced land surface–hydrology model with the Penn State–NCAR MM5 modeling system. Part I: Model implementation and sensitivity. *Mon. Wea. Rev.*, **129**, 569–585.
- , K. Mitchell, J. Schaake, Y. Xue, H.-L. Pan, V. Koren, Q. Duan, and A. Betts, 1996: Modeling of land surface evaporation by four schemes and comparison with FIFE observations (PILPS). *J. Geophys. Res.*, **101** (D3), 7251–7268.
- Chen, T. H., and Coauthors, 1997: Cabauw experimental results from the project for intercomparison of land surface parameterization schemes. *J. Climate*, **10**, 1194–1215.
- Deardorff, J. W., 1978: Efficient prediction of ground surface temperature and moisture with inclusion of a layer of vegetation. *J. Geophys. Res.*, **83**, 1889–1903.
- Deng, A., N. L. Seaman, and J. S. Kain, 2003: A shallow-convective parameterization for mesoscale models. Part I: Submodel description and preliminary application. *J. Atmos. Sci.*, **60**, 34–56.
- Dudhia, J., 1989: Numerical study of convection observed during the winter monsoon experiment using a mesoscale two-dimensional model. *J. Atmos. Sci.*, **46**, 3077–3107.
- GCIP, 1996: GCIP coupled modeling workshop. IGPO Pub. Series 23.
- Ghan, S. J., J. C. Liljegren, W. J. Shaw, J. H. Hubbe, and J. C. Dorman, 1997: Influence of subgrid variability on surface hydrology. *J. Climate*, **10**, 3157–3166.
- Giorgi, F., 1990: Simulation of regional climate using a limited-area model nested in a general circulation model. *J. Climate*, **3**, 941–963.
- , 1991: Sensitivity of simulated summertime precipitation over the United States to different physics parameterizations. *Mon. Wea. Rev.*, **119**, 2870–2888.
- , and R. Avissar, 1997: Representation of heterogeneity effects in earth system modeling: Experience from land surface modeling. *Rev. Geophys.*, **35**, 413–438.
- Gong, W., W. Wang, and H. Wei, 2000: A regional model simulation of the 1991 severe precipitation event over the Yangtze–Huai River Valley. Part I: Precipitation and circulation statistics. *J. Climate*, **13**, 74–92.
- Gutman, G., and A. Ignatov, 1998: The derivation of green vegetation fraction from NOAA/AVHRR data for use in numerical weather prediction models. *Int. J. Remote Sens.*, **19**, 1533–1543.
- Henderson-Sellers, A., Z. L. Yang, and R. E. Dickinson, 1993: The project for intercomparison of land-surface parameterization schemes. *Bull. Amer. Meteor. Soc.*, **74**, 1335–1349.
- Houghton, J. T., and Coauthors, Eds., 1996: *The Science of Climate Change*. Cambridge University Press, 572 pp.
- Hsie, E.-Y., R. A. Anthes, and D. Keyser, 1984: Numerical simulation of frontogenesis in a moist atmosphere. *J. Atmos. Sci.*, **41**, 2581–2594.
- Kain, J. S., and J. M. Fritsch, 1993: Convective parameterization for mesoscale models: The Kain–Fritsch scheme. *The Representation of Cumulus Convection in Numerical Models*, Meteor. Monogr., No. 46, Amer. Meteor. Soc., 165–170.
- Kiehl, J. T., B. A. Boville, B. P. Briegleb, J. J. Hack, P. J. Rasch, and D. L. Williamson, 1996: Description of the NCAR Community Climate Model (CCM3). NCAR Tech. Note NCAR/TN-420+STR, 100 pp.
- Lee, T. J., R. A. Pielke, and P. W. Mielke Jr., 1995: Modeling the clear-sky surface energy budget during FIFE87. *J. Geophys. Res.*, **100**, 25 585–25 593.
- Loveland, T. R., J. W. Merchant, D. O. Ohlen, and J. F. Brown, 1991: Development of a land-cover characteristics database for the conterminous U.S. *Photogramm. Eng. Remote Sens.*, **57**, 1453–1463.
- Miller, D. A., and R. A. White, 1998: A conterminous United States multilayer soil characteristics data set for regional climate and hydrology modeling. *Earth Interactions*, **2**. [Available online at <http://EarthInteractions.org>.]
- Molinari, J., and M. Dudek, 1992: Parameterization of convective

- precipitation in mesoscale numerical models: A critical review. *Mon. Wea. Rev.*, **120**, 326–344.
- NCEP, 1998: Daily Weather Maps. Weekly Series.
- Paegle, J., K. C. Mo, and J. Nogués-Paegle, 1996: Dependence of simulated precipitation on surface evaporation during the 1993 United States summer floods. *Mon. Wea. Rev.*, **124**, 345–361.
- Pan, Z., E. Takle, W. Gutowski, and R. Turner, 1999: Long simulation of regional climate as a sequence of short segments. *Mon. Wea. Rev.*, **127**, 308–321.
- Perkey, D. J., and W. Kreitzberg, 1976: A time-dependent lateral boundary scheme for limited area primitive equation models. *Mon. Wea. Rev.*, **104**, 744–755.
- Sellers, P. J., Y. Mintz, Y. C. Sud, and A. Dalcher, 1986: A simple biosphere model (SiB) for use within general circulation models. *J. Atmos. Sci.*, **43**, 505–531.
- Shao, Y., and A. Henderson-Sellers, 1996: Soil moisture simulation workshop review. *Global Planet. Change*, **12**, 54–90.
- Small, E. E., F. Giorgi, L. C. Sloan, and S. Hostetler, 2001: The effects of desiccation and climatic change on the hydrology of the Aral Sea. *J. Climate*, **14**, 300–322.
- Stensrud, D. J., and J. M. Fritsch, 1994: Mesoscale convective systems in weakly forced large-scale environments. Part III: Numerical simulations and implications for operational forecasting. *Mon. Wea. Rev.*, **122**, 2084–2104.
- Tsvetsinskaya, E. A., L. Mearns, and W. E. Easterling, 2001: Investigating the effect of seasonal plant growth and development in three-dimensional atmospheric simulations. Part II: Atmospheric response to crop growth and development. *J. Climate*, **14**, 711–729.
- Walko, R. L., and Coauthors, 2000: Coupled atmosphere–biophysics–hydrology models for environment modeling. *J. Appl. Meteor.*, **39**, 931–944.
- Wallace, J. M., 1975: Diurnal variations in precipitation and thunderstorm frequency over the conterminous United States. *Mon. Wea. Rev.*, **103**, 406–419.
- Warner, T. T., R. A. Peterson, and R. E. Treadon, 1997: A tutorial on lateral boundary conditions as basic and potentially serious limitations to regional numerical weather prediction. *Bull. Amer. Meteor. Soc.*, **78**, 2599–2617.
- Wen, L., W. Yu, C. A. Lin, M. Beland, R. Benoit, and Y. Delage, 2000: The role of land surface schemes in short-range, high spatial resolution forecasts. *Mon. Wea. Rev.*, **128**, 3605–3617.
- Wetzel, P. J., S. Argentini, and A. Boone, 1996: The role of the land surface in controlling daytime cloud amount: Two case studies in the GCIP-SW area. *J. Geophys. Res.*, **101**, 7359–7370.
- Xue, Y., P. J. Sellers, J. L. Kinter, and J. Shukla, 1991: A simplified biosphere model for global climate studies. *J. Climate*, **4**, 345–364.
- , H. G. Bastable, P. A. Dirmeyer, and P. J. Sellers, 1996a: Sensitivity of simulated surface fluxes to changes in land surface parameterization—A study using ABRACOS data. *J. Appl. Meteor.*, **35**, 386–400.
- , M. J. Fennessy, and P. J. Sellers, 1996b: Impact of vegetation properties on U.S. weather prediction. *J. Geophys. Res.*, **101**, 7419–7430.
- , F. J. Zeng, K. E. Mitchell, Z. Janjic, and E. Rogers, 2001: The impact of land surface processes on simulations of the U.S. hydrological cycle: A case study of the 1993 flood using the SSiB land surface model in the NCEP Eta regional model. *Mon. Wea. Rev.*, **129**, 2833–2860.
- Yang, Z.-L., R. E. Dickinson, A. Henderson-Sellers, and A. J. Pitman, 1995: Preliminary study of spin-up processes in land surface models with the first stage data of Project for Intercomparison of Land Surface Parameterization Schemes phase I(a). *J. Geophys. Res.*, **100**, 16 553–16 578.
- Zhang, D.-L., 1989: The effect of parameterized ice microphysics on the simulation of vortex circulation with a mesoscale hydrostatic model. *Tellus*, **41A**, 132–147.
- , and R. A. Anthes, 1982: A high-resolution model of the planetary boundary layer—Sensitivity tests and comparisons with SESAME-79 data. *J. Appl. Meteor.*, **21**, 1594–1609.
- , and J. M. Fritsch, 1988: Numerical sensitivity experiments of varying physics on the structure, evolution, and dynamics of two mesoscale convective systems. *J. Atmos. Sci.*, **45**, 261–293.
- , and K. Gao, 1989: Numerical simulation of an intense squall line during 10–11 June 1985 PRE-STORM. Part II: Rear inflow, surface pressure perturbations, and stratiform precipitation. *Mon. Wea. Rev.*, **117**, 2067–2094.
- , and E. Altshuler, 1999: The effects of dissipative heating on hurricane intensity. *Mon. Wea. Rev.*, **127**, 3032–3038.
- , E.-Y. Hsie, and M. W. Moncrieff, 1988: A comparison of explicit and implicit predictions of convective and stratiform precipitating weather systems with a meso- $\beta$  scale numerical model. *Quart. J. Roy. Meteor. Soc.*, **114**, 31–60.
- , J. S. Kain, J. M. Fritsch, and K. Gao, 1994: Comments on “Parameterization of convective precipitation in mesoscale numerical models: A critical review.” *Mon. Wea. Rev.*, **122**, 2222–2231.